

Determination of X-ray detection limit and application in perovskite X-ray detectors

Lei Pan

The Ohio State University

Shreetu Shrestha

Los Alamos National Laboratory

Neil Taylor

The Ohio State University

Wanyi Nie

Los Alamos National Laboratory <https://orcid.org/0000-0002-5909-3155>

Lei Cao (✉ cao.152@osu.edu)

The Ohio State University <https://orcid.org/0000-0003-4018-9496>

Article

Keywords: perovskite X-ray detectors, X-ray detection limit

Posted Date: June 1st, 2021

DOI: <https://doi.org/10.21203/rs.3.rs-568088/v1>

License:  This work is licensed under a Creative Commons Attribution 4.0 International License.

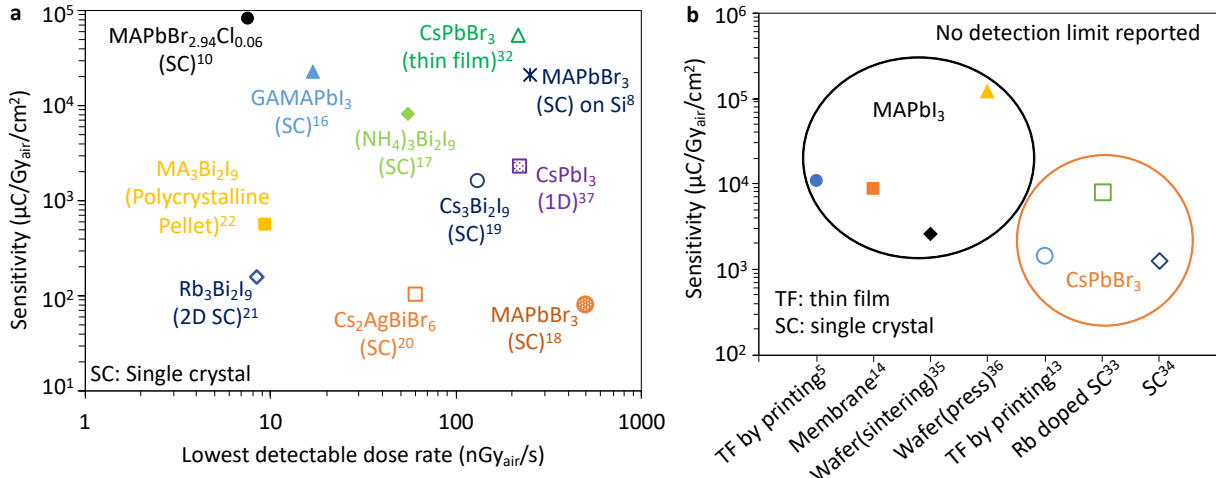
[Read Full License](#)

Version of Record: A version of this preprint was published at Nature Communications on September 6th, 2021. See the published version at <https://doi.org/10.1038/s41467-021-25648-7>.

22 X-ray detectors see wide applications in security inspection, academic research, industry, and
23 medical imaging¹⁻⁴. Detectors that directly convert X-rays into electrical signals are highly desired
24 for X-ray imaging applications due to their higher spatial resolution and greater detection
25 efficiency⁵. Metal halide perovskites emerged recently as promising candidates for direct
26 conversion X-ray detection^{6,7}, with large and tunable bandgap energy (E_g) from 1.6 eV – 3.0 eV
27 that could suppress thermal noises effectively, a large $\mu\tau$ product of $\sim 10^{-4} - 10^{-2}$ cm²/V in favor
28 of charge drifting, a high electron density (*i.e.*, high atomic number and high atom density ~ 4
29 g/cm³) that offers a high X-ray stopping power. The high quality perovskite single crystals can be
30 synthesized from a low-cost solution grown method with excellent performance for X-ray and
31 gamma-ray detection⁸⁻¹², and perovskite thin films can be flexibly deposited or printed onto
32 various substrates in a large area^{5,13-15}.

33 The detection limit of X-ray dose rate (alternatively, lower limit of detection or the lowest
34 detectable dose rate) and sensitivity are important figure of merits for X-ray detectors. Many
35 publications only reported the sensitivity of their perovskite X-ray detectors (**Figure 1**) without
36 discussing on the X-ray lower limit of detection, because the criteria and methods that can correlate
37 the dark current and signal current mathematically with the detection limit have been vague or
38 unjustified, though it has been pointed out qualitatively that a smaller dark current underpins a
39 smaller detection limit^{15,16}. Among the papers that reported detection limits of X-ray dose rate
40 from 0.5 $\mu\text{Gy}_{\text{air}} \text{ s}^{-1}$ down to 7.6 nGy_{air} s⁻¹ for different type of perovskite detectors¹⁵⁻²⁰ (**Figure 1**),
41 many have followed the definition of the detection limit as the lowest X-ray dose rate that can
42 produce a signal three times higher than the noise level^{17,19-22}, which is claimed as the method
43 adopted from the 1975 International Union of Pure and Applied Chemistry (IUPAC) detection
44 limit definition. However, there has been no discussions in these papers, even in the original

45 IUPAC definition²³, whether or not these methods are valid for determining the detection limit of
 46 X-ray detectors working in continuous current mode.



47
 48 **Figure 1. Detection limit and sensitivity of various perovskite X-ray detectors.** The superscript
 49 stands for the reference number. **a.** Perovskite X-ray detectors with sensitivity and detection limit
 50 reported in the literatures. **b.** Sensitivity of MAPbI_3 and all-inorganic CsPbBr_3 X-ray detectors
 51 prepared with different material synthesizing methods and device structures where no detection
 52 limits are reported.

53
 54 In this work, we propose new methods based on a statistical hypothesis testing model to determine
 55 the detection limit of X-ray detectors. Through a review and comparison of the method applied in
 56 various reports^{17,19–22}, the original IUPAC definition²³, and the well-known Currie method²⁴ where
 57 the IUPAC definition stems from, we show that the Currie method, applicable in pulse counting
 58 mode for mass or concentration determination in analytical chemistry and radiochemistry, is a
 59 subset of our proposed methods when sample sizes are reduced. Our proposed methods include a
 60 mathematical expression that correlates the dark current, signal current quantitatively with the
 61 detection limit with sample size effects considered. Without having to measure the X-ray induced

62 signal current, a theoretically conservative *prior* detection limit can be calculated by only dark
63 current measurement through our method, and a *posterior* check of the detectability can be
64 performed after measurement of the X-ray induced signal current to obtain an experimentally
65 determined detection limit.

66 To demonstrate our methods mathematically, we need a calibration factor, which in the case of
67 perovskite X-ray detector is sensitivity, to calculate the *prior* detection limit. We characterized and
68 compared the sensitivity of methylammonium lead triiodide (MAPbI₃) perovskite X-ray detectors
69 with different device architecture and different operation modes, *i.e.*, charge collection mode and
70 charge injection mode. The calculated *prior* detection limit is consistent with the experimentally
71 determined detection limit by *posterior* check of the detectability and the lowest detection limit of
72 $\sim 2.4 \text{ nGy}_{\text{air}}/\text{s}$ is achieved by the detector operated at charge collection mode with charge injection
73 of a device architecture disabled.

74 **Statistical-model based methods for detection limit determination**

75 On the topic of detection limit determination, the Currie formulars, proposed by Currie in 1968²⁴,
76 has been widely cited and universally incorporated into many international standards and
77 regulations²⁵⁻²⁷. Currie method stems from Bernoulli process where atoms are counted over time
78 based on their radioactive decay and assumes Normal distribution for the blank signal X_B , defined
79 as the signal resulting from measurement where the substance sought is absent, and for the gross
80 signal X where the substance sought may exist. Three key parameters related to detection limit are
81 established, that is, critical level L_C , qualitative detection limit L_D , and determination limit for
82 quantification L_Q . If the measured gross signal X is higher than X_c that is equal to the sum of the
83 mean of blank signal $\overline{X_B}$ and the critical level L_C , *i.e.*, $X > X_c$, $X_c = \overline{X_B} + L_C$, a binary decision is
84 made, *i.e.*, “detected” is reported with a false positive probability of α (type I error), otherwise

85 “not detected” is reported with a false negative probability of β (type II error). When both α and
 86 β are set to be 5%, Currie provided a set of convenient working formulars to calculate L_C , L_D , and
 87 L_Q for a large majority of radiation counting applications, which is shown in the widely reprinted
 88 **Table 1**²⁴. Several assumptions are made for **Table 1**: 1) the standard deviation of the blank signal
 89 and the gross signal, denoted as σ_B and σ_Q , respectively, are approximately constant and equal to
 90 each other in the considered range; 2) the relative standard deviation of the signal, that is σ_Q/L_Q ,
 91 is set to be 10% for the determination limit L_Q .

92 **Table 1.** L_C , L_D , and L_Q in Currie method²⁴

	L_C	L_D	L_Q
<i>Paired observations</i>	$2.33 \sigma_B$	$4.65 \sigma_B$	$14.1 \sigma_B$
<i>“Well-known” blank</i>	$1.64 \sigma_B$	$3.29 \sigma_B$	$10 \sigma_B$

Paired observation is defined by Currie as equivalent observations of sample (plus blank) and blank.

“Well-known” blank is defined by Currie as a long history of observations of the blank.

93
 94 Following the Currie method, a detection limit X_D of the gross signal can be directly calculated as
 95 the mean of blank signal $\overline{X_B}$ plus L_D , *i.e.*, $X_D = \overline{X_B} + L_D$. Similarly, the quantification limit is
 96 calculated as $X_Q = \overline{X_B} + L_Q$. To estimate $\overline{X_B}$ and σ_B , a measurement of the blank signal is
 97 necessary. Although the underlying assumption of **Table 1** is Normal distribution in Currie’s
 98 classical paper²⁴, the radioactive decay problems being delt with by Currie’s method originate from
 99 Bernoulli process and end up with Poisson-Normal distribution, defined as the Normal distribution
 100 $\overline{X_B} \sim N(\mu, \sqrt{\mu/n})$ transitioned from Poisson distribution $\overline{X_B} \sim (1/n)\text{Poisson}(n\mu)$ when the mean μ
 101 of Poisson distribution is large (n stands for the sample size, *i.e.*, number of data points). However,
 102 large quantity of X-ray photons emitted from X-ray machine is not a decay phenomenon in nature,

103 nor does the dark current (background signal) of an X-ray detector. On implementation level, the
104 original Currie's definition of the *Paired observations* and the "*Well-known*" blank (**Table 1**) does
105 not explicitly distinguish the sample size n . We interpret the *Paired observations* being the case
106 that acquired only one data point ($n=1$) of the blank signal for $\overline{X_B}$ and σ_B estimation, and the
107 "*Well-known*" blank being the case with many data points ($n \gg 1$) acquired of the blank signal.
108 With the Poisson-Normal distribution assumption, the σ_B can be estimated as $\sqrt{\overline{X_B}}$ when only one
109 data point or one sample ($n=1$) for the *Paired observations* case is acquired. Both *Paired*
110 *observations* and "*Well-known*" blank cases assume implicitly that only one data point of the gross
111 signal would be acquired.

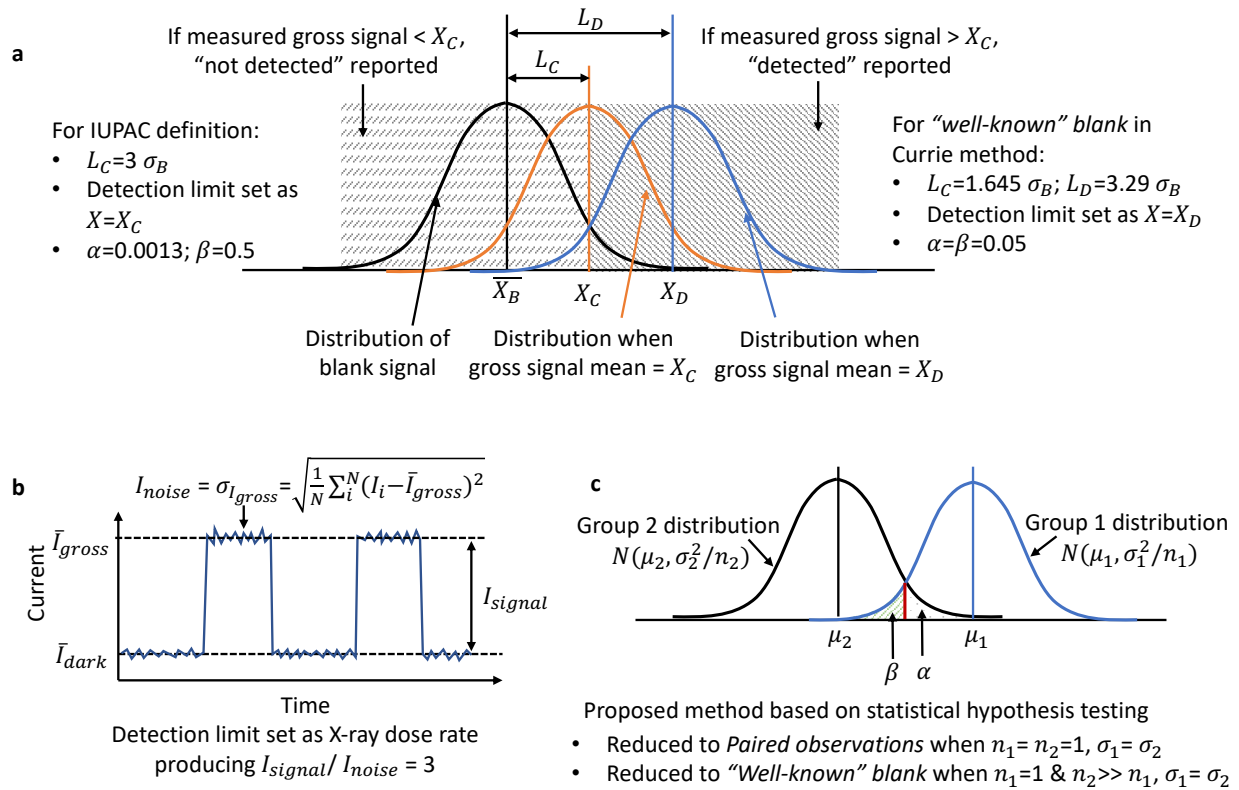
112 Adopting the idea of the Currie method, the IUPAC definition sets the smallest detectable gross
113 signal $X = X_C$ that is higher than the mean of the blank signal $\overline{X_B}$ for a difference of $3\sigma_B$ ²³, *i.e.*,
114 $X_C = \overline{X_B} + 3\sigma_B$, which is equivalent to setting $L_C = 3\sigma_B$. Consequently, the IUPAC defined
115 detection limit ensures a type I error $\alpha = 0.13\%$, but a type II error $\beta = 50\%$ ^{25,28}. The IUPAC
116 definition also assumes implicitly only one sample or data point for the gross signal would be
117 acquired as it is descended from the Currie method. The relationship of the relevant parameters for
118 the "*Well-known*" blank in Currie method and the IUPAC definition are illustrated in **Figure 2a**.

119 Although the method for X-ray detection limits found in various publications^{17,19-22} claims the use
120 of IUPAC definitions in determining the detection limit of perovskite X-ray detectors, none have
121 paid attention to the fact that the large data points acquired by an X-ray detector working in current
122 mode is different than that limited data points defined in Currie's paper. We show there is a
123 discrepancy between IUPAC definition and the method being used in the publications^{17,19-22}
124 reporting perovskite for X-ray detection, as shown in **Figure 2b**. The signal current I_{signal} is
125 calculated as the difference between the mean gross current $\overline{I_{gross}}$ measured with X-ray and the

126 mean dark current \bar{I}_{dark} without X-ray, *i.e.*, $I_{signal} = |\bar{I}_{gross} - \bar{I}_{dark}|$. The standard deviation of
 127 the gross current, termed as noise current I_{noise} , is calculated with equation (1), where N is the
 128 large number of data points measured of the digitized gross current readout. With the definitions
 129 above, the detection limit for an X-ray detector is the X-ray dose rate that produces electric current
 130 at a Signal-to-Noise Ratio (SNR) of 3 with SNR defined as I_{signal}/I_{noise} .

$$I_{noise} = \sqrt{\frac{1}{N} \sum_i^N (I_i - \bar{I}_{gross})^2} \quad (1)$$

131 By comparison, we found that $I_{signal} = |\bar{I}_{gross} - \bar{I}_{dark}|$ corresponds to the $X - \bar{X}_B = 3\sigma_B$ in the
 132 IUPAC definition. However, the IUPAC definition assumes only one data point is taken for the
 133 gross signal, contrary to a large number of data points usually taken for the gross current of X-ray
 134 detector with a continuously sampled current readout, *i.e.*, \bar{I}_{gross} . Besides, in the IUPAC
 135 definition, the standard deviation of the blank signal, σ_B , is used, as it assumes $\sigma_B = \sigma_Q$ following
 136 the Currie method. However, I_{noise} is taken from the standard deviation of the gross signal (**Figure**
 137 **2b**), *i.e.*, σ_Q , that may not be equal to σ_B .



138

139 **Figure 2. Review and comparison of different methods for detection limit determination. a.**

140 The "Well-known" blank in the Currie method and the IUPAC definition. **b.** The method used in

141 various reports^{17,19-22} for perovskite X-ray dose rate detection limit determination. **c.** The method

142 proposed in this work based on statistical model, which reduces to the Currie method with certain

143 pre-assumptions.

144

145 Given such discrepancies, a method that takes into account the large number of data points

146 measured of the dark current and the gross current as well as their different standard deviations is

147 needed to accurately determine the detection limit of X-ray detectors working in current mode.

148 Here, we introduce two equations from the statistical hypothesis testing model for comparing the

149 means of two normally distributed samples (*i.e.*, physical parameters) of unequal sample size (*i.e.*,

150 number of data points) for detection limit determination. The equations (2) and (3) (named as

151 Detection Limit (DL) equations thereafter in this paper) are well-established equations that can be
 152 found in statistical theory books²⁹. In DL equations, n_1 , n_2 are the sample size of the Group 1 and
 153 Group 2, respectively. $\Delta = |\mu_1 - \mu_2|$ is the detection limit. (μ_1, σ_1^2) , (μ_2, σ_2^2) are the means and
 154 variances of the two respective groups following Normal distribution. $k = n_2/n_1$ is the ratio of
 155 the two sample sizes. The $z_{1-\alpha}$ and $z_{1-\beta}$ are the Z-score corresponding to type I error α and type
 156 II error β , respectively, for one-sided test. The relevant parameters are illustrated in **Figure 2c**.
 157 The equations (2) and (3) can be rearranged to cancel k , yielding equation (4), which is another
 158 form of the DL equations.

$$n_1 = \frac{(\sigma_1^2 + \sigma_2^2/k)(z_{1-\alpha} + z_{1-\beta})^2}{\Delta^2} \quad (2)$$

$$n_2 = \frac{(k \sigma_1^2 + \sigma_2^2)(z_{1-\alpha} + z_{1-\beta})^2}{\Delta^2} \quad (3)$$

$$\Delta = |\mu_1 - \mu_2| = (z_{1-\alpha} + z_{1-\beta}) \sqrt{\frac{\sigma_1^2}{n_1} + \frac{\sigma_2^2}{n_2}} \quad (4)$$

159 Assuming Group 1 and Group 2 represent the gross signal and the blank signal throughout in this
 160 work (equivalently vice versa), respectively, then a *prior* detection limit $\Delta = |\mu_1 - \mu_2|$ can be
 161 calculated with the measured blank signal of Group 2, *i.e.*, (μ_2, σ_2^2) and n_2 from the DL equations,
 162 with some necessary pre-assumptions. We make assumptions consistent with the Currie method
 163 and show that the DL equations is same as Currie formulars when sample sizes are being reduced.
 164 We set $\alpha=\beta=0.05$, corresponding to $z_{1-\alpha} = z_{1-\beta} = 1.645$, and assume $\sigma_1^2 = \sigma_2^2$. The effect of
 165 sample size on detection limit comes into play by controlling the value of $k = n_2/n_1$. If we set
 166 $n_2=n_1=1$, we have $k=1$. Then the DL equations reduce to $\Delta^2 = (\sigma_1^2 + \sigma_2^2)(z_{1-\alpha} + z_{1-\beta})^2$. With
 167 the assumptions of $\sigma_1^2=\sigma_2^2$ and $z_{1-\alpha} = z_{1-\beta} = 1.645$, we have $\Delta = |\mu_1 - \mu_2| = \sqrt{2}\sigma_2 * 3.29 =$

168 $4.65\sigma_2$, which is the detection limit L_D in *Paired observations* case in Currie's classical paper²⁴
169 **(Table 1)**. If we set $n_1=1$ and $n_2 \gg n_1$, that is, $k = n_2/n_1 \gg 1$, so that $\sigma_1^2 \gg \sigma_2^2/k$ or $k \sigma_1^2 \gg \sigma_2^2$,
170 then the DL equations reduce to $\Delta^2 = \sigma_1^2(z_{1-\alpha} + z_{1-\beta})^2$. With the same assumptions, we have
171 $\Delta = |\mu_1 - \mu_2| = 3.29\sigma_2$, which is the detection limit L_D in "*Well-known*" *blank* case in Currie's
172 paper²⁴ **(Table 1)**.

173 An important understanding of the DL equations is that the detection limit can be effectively
174 further reduced by increasing the sample size, *i.e.*, n_1 or n_2 , which however often means increased
175 cost for the prolonged experiment. For the case of X-ray detector current measurement, the sample
176 size of the blank signal can be very large, as the dark current can be measured off-line for a long
177 period of time without inducing much cost. In comparison, the sample size of the gross signal, *i.e.*,
178 gross current with X-ray on, is better to be kept as small as needed to reduce the cumulative X-ray
179 dose to patients. With this consideration, we recommend a theoretically conservative *prior*
180 calculated detection limit of perovskite X-ray detectors with preset value of $n_1=1$ and $n_2 \gg n_1$,
181 that is, $\Delta = |\mu_1 - \mu_2| = 3.29\sigma_2$, equivalent to "*Well-known*" *blank* in Currie method. For other
182 practical measurement cases where a preset value of $n_1 > 1$ is used with $n_2 \gg n_1$, the *prior*
183 detection limit can be further reduced through calculation of $\Delta^2 = \sigma_1^2(z_{1-\alpha} + z_{1-\beta})^2/n_1$.

184 The assumption $\sigma_1^2 = \sigma_2^2$ is reasonable in most cases if the signal to be detected is small and is
185 approaching to the level of detection limit. Generally speaking, σ_1^2 is not necessarily equal to σ_2^2 .
186 Without an assumption of the relationship between σ_1^2 and σ_2^2 , a *prior* calculation of the detection
187 limit cannot be performed, but we can still do a *posterior* check of the detectability after both blank
188 signal and gross signal are acquired. Specifically, with n_1 , n_2 , σ_1^2 , σ_2^2 determined from the
189 measurement, the theoretical detection limit $\Delta = |\mu_1 - \mu_2|$ can be calculated from the DL
190 equations with preset values of $z_{1-\alpha}$ and $z_{1-\beta}$. Besides, a difference of the two mean values can

191 be directly obtained from the measurement. By comparison, if the measured mean value difference
192 is larger than the calculated theoretical detection limit Δ , the signal is detected with the preset false
193 positive probability α and the false negative probability β satisfied, otherwise the preset false
194 positive and false negative probability cannot be satisfied.

195 The method for detection limit of X-ray dose rate in other reports^{17,19-22} essentially can be
196 attributed to a *posterior* check of the detectability. The $I_{signal} = |\bar{I}_{gross} - \bar{I}_{dark}|$ is the counterpart
197 to $\Delta = |\mu_1 - \mu_2|$, while $I_{noise} = \sigma_{I_{gross}}$ is equivalent to the standard deviation of the gross signal
198 σ_1 , and $I_{signal}/I_{noise}=3$ corresponds to setting $z_{1-\alpha} + z_{1-\beta} = 3$. However, the method used in
199 these reports itself is inappropriate because mathematically it does not consider the effect of sample
200 size on the detection limit, and, from the underling physics perspective, the X-ray detector's
201 current readout is not a Bernoulli process. Similar to the detection limit, the determination limit
202 for quantification by *prior* calculation or by *posterior* check can be obtained by setting $z_{1-\alpha} +$
203 $z_{1-\beta} = 10$ in the DL equations that is consistent with a relative standard deviation of 10% in Currie
204 method. For a fixed value of $z_{1-\alpha} + z_{1-\beta} = 10$, the larger the sample size, *i.e.*, n_1 or n_2 , the smaller
205 the $\Delta = |\mu_1 - \mu_2|$, and hence the lower the determination limit for quantification.

206 Mathematically, the DL equations extend the Currie method by taking into account explicitly the
207 effect of sample size and different standard deviations of both blank and gross signal on detection
208 limit, which makes these new methods applicable to X-ray detectors working in continuous current
209 mode where a large number of data points are usually sampled for the dark and gross current.

210

211 **Sensitivity of MAPbI₃ detector at different working mode**

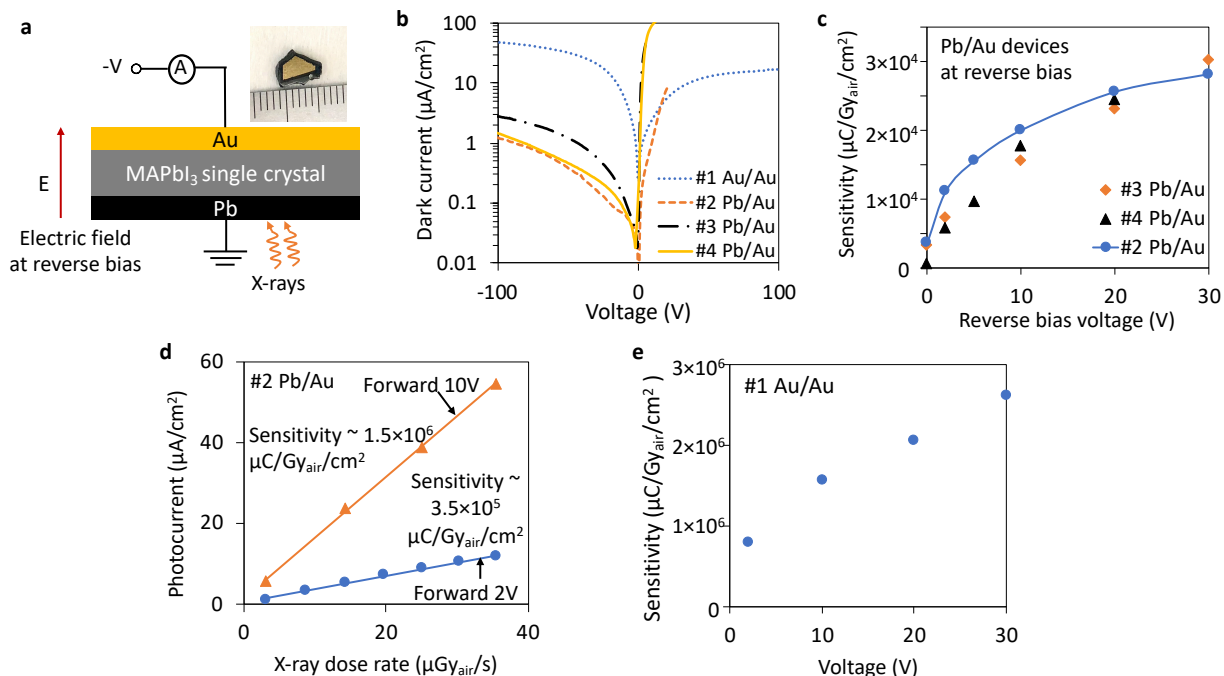
212 For perovskite X-ray detectors, the directly measurable parameter from a meter reading is
213 photocurrent, while the X-ray dose rate is not directly measurable. The detection limit of the
214 directly measurable parameter can be simply converted to the detection limit of the parameter not
215 directly measurable with a calibration factor^{24,28}. Hence, the detection limit of X-ray dose rate
216 (again, interchangeably, the lowest detectable dose rate) D_{limit} is obtained by $D_{limit} = I_{limit}/(A * s)$,
217 where I_{limit} is the *prior* calculated detection limit of the directly measurable photocurrent, A
218 is the detector area and s is the detector sensitivity under the condition where the photocurrent
219 measurement is taken. To obtain a *prior* calculated D_{limit} , we need to first calculate the sensitivity
220 of the X-ray detector.

221 It has been reported that organic thin film based X-ray detectors could have wide ranging
222 sensitivity depending on which mode the detector is operated^{30,31}. The charge injection mode can
223 produce giant sensitivity due to the photoconductive gain effect but with a large dark current. In
224 comparison, the charge collection mode has relatively smaller sensitivity but with a smaller dark
225 current due to the suppression of charge injection. Here, we calculate the sensitivity of perovskite
226 X-ray detectors working at different mode, which also serves to demonstrate the influence of
227 device architecture and hence the detector operation mode on sensitivity and detection limit.

228 We are illustrating the concept with four devices made of MAPbI₃ single crystal with different
229 architectures (see **Figure S1** and **Figure S2** for material characterizations). The #1 device has an
230 Au/MAPbI₃/Au structure (shortened as Au/Au), whereas the #2, #3, and #4 device have
231 Pb/MAPbI₃/Au structure (shortened as Pb/Au). The dimensions of the devices are listed in **Table**
232 **S1**. The surface of MAPbI₃ single crystal is typically p-type¹⁶, which results in Ohmic and Schottky
233 junction when forming contact with high and low work function metal, respectively¹¹. The Pb/Au
234 devices show a clear current rectifying behavior with a suppressed dark current at reverse bias

235 (electric field direction from Pb to Au) (**Figure 3a**, and **Figure 3b**). In comparison, the Au/Au
236 device is a double Ohmic structure, showing negligible current rectifying behavior and hence large
237 dark current under both biasing directions (**Figure 3b**). According to the I-V behavior, the MAPbI₃
238 detector with Pb/Au structure works at charge collection mode when reversely biased, whereas it
239 works at charge injection mode when forward biased. The MAPbI₃ detector with Au/Au structure
240 works at charge injection mode under either bias voltage direction (see **Figure S3** for energy band
241 diagram of respective device structures).

242 The sensitivity of all MAPbI₃ detectors were measured by collecting hole dominantly induced
243 signal, *e.g.*, X-rays irradiating the Pb electrode when the Pb/Au device is reversely biased (**Figure**
244 **3a**), as the X-ray photons have limited penetration depth in MAPbI₃ (see **Figure S4**). The
245 sensitivity of the reversely biased Pb/Au devices working at charge collection mode is around 1-2
246 orders of magnitude smaller than the devices working at charge injection mode (see **Figure S5**
247 **and Figure S6** for sensitivity calculation procedures). It can be seen that the device architecture
248 and the associated detector operational mechanisms play critical role in controlling the sensitivity,
249 which, however, is often overlooked when sensitivity values are being reported for perovskite X-
250 ray detectors. Although the reported sensitivities from numerous perovskite X-ray detectors,
251 including single crystals^{8,10,16–20,32–34}, thin films^{5,13,14,35,36}, and 2D/1D perovskites^{21,22,37}, are in a
252 wide range covering six orders of magnitude, from 80 $\mu\text{C Gy}_{\text{air}}^{-1} \text{cm}^{-2}$ to $1.22 \times 10^5 \mu\text{C Gy}_{\text{air}}^{-1} \text{cm}^{-2}$
253 (**Figure 1**), a giant sensitivity does not necessarily indicate a superior material or device quality
254 without an equitable ground of detector operational mechanisms.

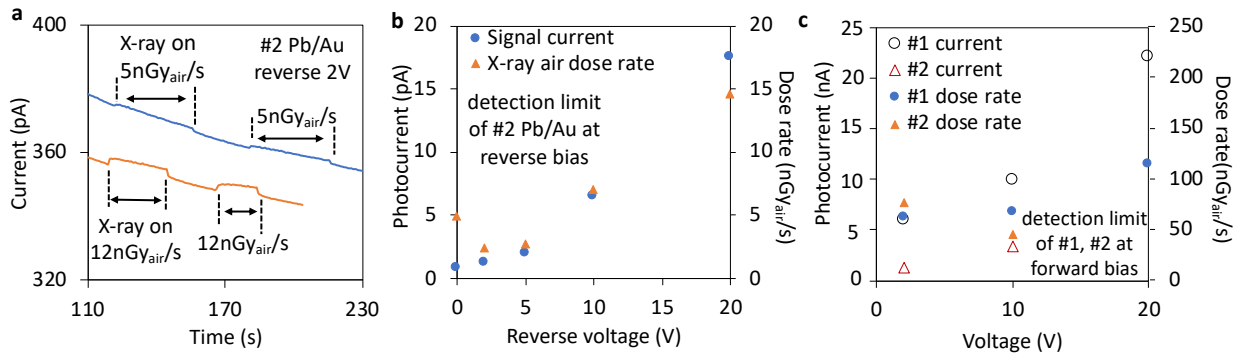


255
 256 **Figure 3. Sensitivity measurement and comparison of MAPbI₃ single crystal devices at**
 257 **different working mode. a.** Experiment setup for reverse bias operation of the Pb/Au devices and
 258 the hole dominantly induced signal collection. **b.** Dark I-V characterization of the devices. **c.**
 259 Sensitivity of the reversely biased Pb/Au devices working at charge collection mode. **d.**
 260 Photocurrent and sensitivity of the forward biased #2 Pb/Au device working at charge injection
 261 mode. **e.** Sensitivity of the Au/Au device working at charge injection mode.

262
 263 **Calculation of MAPbI₃ X-ray dose rate detection limit**

264 The *prior* calculation of the detection limit requires the measurement of sensitivity as calibration
 265 factor. In comparison, the detection limit estimation by *posterior* check of the detectability can be
 266 performed experimentally by lowering the X-ray dose rate successively to the level close to the
 267 detection limit, which does not require a measured sensitivity. We demonstrate here detection limit
 268 determination mathematically by both *prior* calculation and by *posterior* check.

269 The X-ray induced photocurrent is more eminent at an X-ray dose rate of 12 nGy_{air}/s than that at
 270 5 nGy_{air}/s for #2 Pb/Au device under reverse 2 V (**Figure 4a**), and it can be expected that the
 271 photocurrent will be indiscernible from dark current by visual inspection if the dose rate is further
 272 reduced. We calculate a theoretically conservative *prior* detection limit $\Delta = |\mu_1 - \mu_2| = 3.29\sigma_2$
 273 with preset value of $n_1=1$ and $n_2 \gg n_1$, as aforementioned. The dark current standard deviation,
 274 *i.e.*, σ_2 , is calculated to be ~ 0.376 pA, which yields a detection limit of the directly measurable
 275 photocurrent of $I_{limit} = 3.29\sigma_2 = 1.24$ pA. After conversion, the X-ray dose rate detection limit is
 276 calculated to be $D_{limit} = I_{limit}/(A * s) = 2.4$ nGy_{air}/s, where electrode area is $A = 0.0468$ cm² and
 277 sensitivity is $s = 11,180$ $\mu\text{C Gy}_{air}^{-1} \text{cm}^{-2}$ at reverse 2 V of the #2 Pb/Au device.



278

279 **Figure 4. *Prior* calculated detection limit for MAPbI₃ detectors working at different mode.**

280 **a.** Experimentally measured current response of reversely biased #2 Pb/Au device to X-ray dose
 281 rate approaching the detection limit. *Prior* calculated detection limit of photocurrent and X-ray
 282 dose rate in air for the **b.** reversely biased #2 Pb/Au device at charge collection mode, and for the
 283 **c.** #1 Au/Au device and forward biased #2 Pb/Au device at charge injection mode.

284

285 A *posterior* check of the detectability can be performed for the measurement with dose rate of 5
 286 nGy_{air}/s. We collected a large number of digitized data points for the dark current so that n_2 in the

287 DL equations is very large (typically ~ 500), which satisfies $\sigma_1^2 \gg \sigma_2^2/k$ or $k \sigma_1^2 \gg \sigma_2^2$. We have
 288 $n_1=17$ data points for a specific gross current measurement with X-ray dose rate at 5 nGy_{air}/s. The
 289 standard deviation of the gross current, *i.e.*, σ_1 , is calculated to be ~ 0.468 pA. Then we can
 290 calculate a theoretical detection limit for this specific measurement to be $\Delta = |\mu_1 - \mu_2| = 0.37$ pA
 291 that satisfies $z_{1-\alpha} = z_{1-\beta} = 1.645$. Meanwhile, the measured difference of the mean dark current
 292 and the mean gross current is 5.9 pA. As the measured difference is larger than the calculated
 293 theoretical detection limit, the X-ray dose rate of 5 nGy_{air}/s is considered “detected” satisfying the
 294 preset $z_{1-\alpha} = z_{1-\beta} = 1.645$, which corroborates the *prior* calculated detection limit of 2.4 nGy_{air}/s.
 295 Using the same *prior* calculation method, the detection limits of the reversely bias #2 Pb/Au device
 296 at charge collection mode were obtained (**Figure 4b**). The directly measured X-ray induced
 297 photocurrent has an increased detection limit as reverse bias voltage increases, because the
 298 increased reverse bias leads to the increased mean value and standard deviation of the dark current.
 299 Although the photocurrent detection limit I_{limit} monotonically increases as function of reverse
 300 bias, the X-ray dose rate detection limit $D_{limit} = I_{limit}/(A * s)$ dose not necessarily increases
 301 monotonically since the sensitivity s also increases as reverse bias increases (**Figure 3c**). The
 302 *posterior* check of the detectability also supports the *prior* calculated detection limit (**Figure S7**).
 303 Compared to reversely biased Pb/Au devices at charge collection mode, the *prior* calculated
 304 detection limit of the X-ray induced photocurrent increased by ~ 3 orders of magnitude for the
 305 forward biased #2 Pb/Au device at charge injection mode (**Figure 4c**), as a consequence of the
 306 large dark current under forward bias. The #1 Au/Au device at charge injection mode has a
 307 photocurrent detection limit at the same level as of the forward biased #2 Pb/Au device. Despite
 308 the photocurrent detection limit increased dramatically by ~ 1000 times for the devices working at
 309 charge injection mode, the X-ray dose rate detection limit only increased by ~ 10 folds, because

310 the sensitivity of the devices at charge injection mode are ~ 2 orders of magnitude higher than the
311 devices at charge collection mode.

312 **Conclusions**

313 We proposed new methods, including the adoption of mathematical equations for detection limit
314 determination, sample size effects on the detection limit, a *prior* calculation and a *posterior* check
315 of the detection limit, based on well-established statistical model to determine the detection limit
316 for X-ray detectors working in continuous current mode where Normal distribution is followed. In
317 comparison, the established Currie method deals with time-accumulated photon counting
318 problems that are routed from Bernoulli process, described by Binomial distribution. Although
319 photon counting is approximated by Poisson distribution and finally Poisson-Normal distribution
320 when the number of counts in one data point are large, the X-ray phonons being produced by an
321 X-ray machine and the dark current of X-ray detector do not belong to Bernoulli process and they
322 follow Normal distribution in nature.

323 This method mathematically includes different sample size and standard deviation of both blank
324 and gross signal, which reduces to the subset of Currie formulars with assumptions on the sample
325 sizes and standard deviations. A *prior* calculation and a *posterior* check can be used to determine
326 or verify the detection limit accordingly. The *prior* calculation method can be simply performed
327 as summarized in **Table 2**. A *prior* calculated detection limit as low as ~ 2.4 nGy_{air}/s at reverse 2V
328 was achieved by our MAPbI₃ single crystal detector.

329

330

331

Table 2. The *prior* calculation method of detection limit $\Delta = |\mu_1 - \mu_2|$

Detection Limit equations	$n_2=n_1$	$n_2 \gg n_1$
$\Delta = (z_{1-\alpha} + z_{1-\beta}) \sqrt{\frac{\sigma_1^2}{n_1} + \frac{\sigma_2^2}{n_2}}$	$\Delta = 4.65 \frac{\sigma_2}{\sqrt{n_1}}$	$\Delta = 3.29 \frac{\sigma_2}{\sqrt{n_1}}$
	$\Delta = 4.65 \sigma_2$ (reduce to <i>Paired observations</i> ²⁴ when $n_1=1$)	$\Delta = 3.29 \sigma_2$ (reduce to “ <i>Well-known</i> ” <i>blank</i> ²⁴ when $n_1=1$)

Assumptions: 1) gross signal standard deviation $\sigma_1 =$ blank signal standard deviation σ_2 . 2) $\alpha=\beta=5\%$ ($z_{1-\alpha}=z_{1-\beta}=1.645$). 3) n_1 and n_2 are the sample size of gross signal and blank signal, respectively.

332

333 Sensitivity is needed for the *prior* calculation of the X-ray dose rate detection limit. We measured
 334 and compared the sensitivity of MAPbI₃ single crystal X-ray detectors with different operational
 335 mechanisms, *i.e.*, charge collection mode and charge injection mode, which demonstrates the
 336 critical role of device architecture and operation modes in controlling the perovskite X-ray detector
 337 sensitivity. When comparing sensitivity of different perovskite X-ray detectors for material quality
 338 and device performance comparison, it is important to highlight the device working mode for a
 339 fair competition. Our work could facilitate effective design and characterization of perovskite X-
 340 ray detectors for medical imaging or other non-perovskite photoelectric sensor systems.

341

342 References

- 343 1. Hoheisel, M. Review of medical imaging with emphasis on X-ray detectors. *Nucl.*
 344 *Instruments Methods Phys. Res. Sect. A Accel. Spectrometers, Detect. Assoc. Equip.* (2006)
 345 doi:10.1016/j.nima.2006.01.123.
- 346 2. Belev, G. & Kasap, S. O. Amorphous selenium as an X-ray photoconductor. in *Journal of*
 347 *Non-Crystalline Solids* (2004). doi:10.1016/j.jnoncrysol.2004.08.070.
- 348 3. Panta, R. K. *et al.* First human imaging with MARS photon-counting CT. in *2018 IEEE*
 349 *Nuclear Science Symposium and Medical Imaging Conference, NSS/MIC 2018 -*
 350 *Proceedings* (2018). doi:10.1109/NSSMIC.2018.8824513.
- 351 4. Kasap, S. *et al.* Amorphous and polycrystalline photoconductors for direct conversion flat
 352 panel x-ray image sensors. *Sensors* (2011) doi:10.3390/s110505112.
- 353 5. Kim, Y. C. *et al.* Printable organometallic perovskite enables large-area, low-dose X-ray

- 354 imaging. *Nature* (2017) doi:10.1038/nature24032.
- 355 6. Wei, H. & Huang, J. Halide lead perovskites for ionizing radiation detection. *Nat. Commun.*
356 10, 1–12 (2019).
- 357 7. Yang, Y., Su, Y., Ma, W. & Yang, Y. M. Perovskite semiconductors for direct X-ray
358 detection and imaging. *Journal of Semiconductors* (2020) doi:10.1088/1674-
359 4926/41/5/051204.
- 360 8. Wei, W. *et al.* Monolithic integration of hybrid perovskite single crystals with heterogenous
361 substrate for highly sensitive X-ray imaging. *Nat. Photonics* (2017)
362 doi:10.1038/nphoton.2017.43.
- 363 9. Pan, L., Feng, Y., Kandlakunta, P., Huang, J. & Cao, L. R. Performance of Perovskite
364 CsPbBr₃ Single Crystal Detector for Gamma-Ray Detection. *IEEE Trans. Nucl. Sci.* **67**,
365 443–449 (2020).
- 366 10. Wei, H. *et al.* Dopant compensation in alloyed CH₃NH₃PbBr_{3-x} Cl_x perovskite single
367 crystals for gamma-ray spectroscopy. *Nat. Mater.* (2017) doi:10.1038/nmat4927.
- 368 11. He, Y. *et al.* Resolving the Energy of γ -Ray Photons with MAPbI₃ Single Crystals. *ACS*
369 *Photonics* (2018) doi:10.1021/acsp Photonics.8b00873.
- 370 12. Pan, L., Feng, Y., Huang, J. & Cao, L. R. Comparison of Zr, Bi, Ti, and Ga as Metal
371 Contacts in Inorganic Perovskite CsPbBr₃ Gamma-Ray Detector. *IEEE Trans. Nucl. Sci.*
372 (2020) doi:10.1109/TNS.2020.3018101.
- 373 13. Liu, J. *et al.* Flexible, Printable Soft-X-Ray Detectors Based on All-Inorganic Perovskite
374 Quantum Dots. *Adv. Mater.* (2019) doi:10.1002/adma.201901644.
- 375 14. Zhao, J. *et al.* Perovskite-filled membranes for flexible and large-area direct-conversion X-
376 ray detector arrays. *Nat. Photonics* (2020) doi:10.1038/s41566-020-0678-x.
- 377 15. Tsai, H. *et al.* A sensitive and robust thin-film x-ray detector using 2D layered perovskite
378 diodes. *Sci. Adv.* (2020) doi:10.1126/sciadv.aay0815.
- 379 16. Huang, Y. *et al.* A-site Cation Engineering for Highly Efficient MAPbI₃ Single-Crystal X-
380 ray Detector. *Angewandte Chemie - International Edition* (2019)
381 doi:10.1002/anie.201911281.
- 382 17. Zhuang, R. *et al.* Highly sensitive X-ray detector made of layered perovskite-like
383 (NH₄)₃Bi₂I₉ single crystal with anisotropic response. *Nat. Photonics* (2019)
384 doi:10.1038/s41566-019-0466-7.
- 385 18. Wei, H. *et al.* Sensitive X-ray detectors made of methylammonium lead tribromide
386 perovskite single crystals. *Nat. Photonics* **10**, 333–339 (2016).
- 387 19. Zhang, Y. *et al.* Nucleation-controlled growth of superior lead-free perovskite Cs₃Bi₂I₉
388 single-crystals for high-performance X-ray detection. *Nat. Commun.* (2020)
389 doi:10.1038/s41467-020-16034-w.
- 390 20. Pan, W. *et al.* Cs₂AgBiBr₆ single-crystal X-ray detectors with a low detection limit. *Nat.*
391 *Photonics* (2017) doi:10.1038/s41566-017-0012-4.
- 392 21. Xia, M. *et al.* Unveiling the Structural Descriptor of A₃B₂X₉ Perovskite Derivatives toward
393 X-Ray Detectors with Low Detection Limit and High Stability. *Adv. Funct. Mater.* (2020)
394 doi:10.1002/adfm.201910648.
- 395 22. Tie, S. *et al.* Robust Fabrication of Hybrid Lead-Free Perovskite Pellets for Stable X-ray
396 Detectors with Low Detection Limit. *Adv. Mater.* (2020) doi:10.1002/adma.202001981.
- 397 23. Nomenclature, symbols, units and their usage in spectrochemical analysis—II. data
398 interpretation Analytical chemistry division. *Spectrochim. Acta Part B At. Spectrosc.* **33**,
399 241–245 (1978).

- 400 24. Currie, L. A. Limits for Qualitative Detection and Quantitative Determination: Application
401 to Radiochemistry. *Anal. Chem.* (1968) doi:10.1021/ac60259a007.
- 402 25. Currie, L. A. Nomenclature in evaluation of analytical methods including detection and
403 quantification capabilities (IUPAC Recommendations 1995). *Pure Appl. Chem.* **67**, 1699–
404 1724 (1995).
- 405 26. Currie, L. A. *Lower limit of detection: definition and elaboration of a proposed position for*
406 *radiological effluent and environmental measurements.* (1984).
- 407 27. Currie, L. A. Detection in analytical chemistry. Importance, theory, and practice. (1988).
- 408 28. Long, G. L. & Winefordner, J. D. Limit of Detection: A Closer Look at the IUPAC
409 Definition. *Anal. Chem.* (1983) doi:10.1021/ac00258a001.
- 410 29. Bernard, R. Fundamentals of Biostatistics, (5th edition). *Boston, PWS Publishers* (2000).
- 411 30. Ciavatti, A. *et al.* Dynamics of direct X-ray detection processes in high-Z Bi₂O₃
412 nanoparticles-loaded PFO polymer-based diodes. *Appl. Phys. Lett.* (2017)
413 doi:10.1063/1.4986345.
- 414 31. Basiricò, L. *et al.* Direct X-ray photoconversion in flexible organic thin film devices
415 operated below 1 v. *Nat. Commun.* (2016) doi:10.1038/ncomms13063.
- 416 32. Pan, W. *et al.* Hot-Pressed CsPbBr₃ Quasi-Monocrystalline Film for Sensitive Direct X-ray
417 Detection. *Adv. Mater.* (2019) doi:10.1002/adma.201904405.
- 418 33. Li, J. *et al.* Rubidium Doping to Enhance Carrier Transport in CsPbBr₃ Single Crystals for
419 High-Performance X-Ray Detection. *ACS Appl. Mater. Interfaces* (2020)
420 doi:10.1021/acsami.9b14772.
- 421 34. Zhang, H. *et al.* High-sensitivity X-ray detectors based on solution-grown caesium lead
422 bromide single crystals. *J. Mater. Chem. C* (2020) doi:10.1039/c9tc05490a.
- 423 35. Shrestha, S. *et al.* High-performance direct conversion X-ray detectors based on sintered
424 hybrid lead triiodide perovskite wafers. *Nat. Photonics* (2017)
425 doi:10.1038/nphoton.2017.94.
- 426 36. Hu, M. *et al.* Large and Dense Organic-Inorganic Hybrid Perovskite CH₃NH₃PbI₃ Wafer
427 Fabricated by One-Step Reactive Direct Wafer Production with High X-ray Sensitivity.
428 *ACS Appl. Mater. Interfaces* (2020) doi:10.1021/acsami.9b23158.
- 429 37. Zhang, B. Bin *et al.* High-Performance X-ray Detection Based on One-Dimensional
430 Inorganic Halide Perovskite CsPbI₃. *J. Phys. Chem. Lett.* (2020)
431 doi:10.1021/acs.jpcllett.9b03523.
- 432 38. Rao, H.-S., Chen, B.-X., Wang, X.-D., Kuang, D.-B. & Su, C.-Y. A micron-scale laminar
433 MAPbBr₃ single crystal for an efficient and stable perovskite solar cell. *Chem. Commun.*
434 **53**, 5163–5166 (2017).
- 435 39. Liu, Y. *et al.* Thinness-and shape-controlled growth for ultrathin single-crystalline
436 perovskite wafers for mass production of superior photoelectronic devices. *Adv. Mater.* **28**,
437 9204–9209 (2016).
- 438

439 **Acknowledgments:** This work was supported by the U.S. Department of the Defense, Defense
440 Threat Reduction Agency under Grant HDTRA1-19-1-0024 and partially supported by the U. S.
441 Department of Energy / National Nuclear Security Administration under Award Number DE-
442 NA0003921. W.N. and S.S. acknowledges the Los Alamos National Laboratory's LDRD Mission

443 Foundation Project. Their work was performed, in part, at the Center for Integrated
444 Nanotechnologies, an Office of Science User Facility operated for the U.S. Department of Energy,
445 Office of Science by Los Alamos National Laboratory (Contract 89233218CNA000001) and
446 Sandia National Laboratory (Contract DE-NA-0003525). We thank Miss. Qingyu Chen, Ph.D
447 student at The Ohio State University, for the helpful discussion of the relevant statistical theory.

448 **Author contributions:** L.R.C. and L.P. conceived the idea and proposed the statistical methods.
449 L.P. designed experiments and characterized detector performance. W.N. and S.S. synthesized,
450 characterized the single crystals and fabricated the devices. N.T. contributed to the discussion of
451 detection limit. L.P., L.R.C., and W.N. wrote the manuscript. All authors discussed the results and
452 commented on the manuscript.

453 **Competing interests:** The authors declare no competing interests.

454 **Data and materials availability:** All data is available in the main text or the Supplementary
455 Information.

456

457 **Methods**

458 **Crystal growth.** MAPbI₃ thin single crystals were grown using the space confined inverse
459 temperature crystal growth method as reported in literatures^{38,39}. Briefly, an equimolar ratio of
460 methylammonium iodide (MAI) and lead iodide (PbI) are dissolved in γ butyrolactone (GBL) to
461 obtain a 1.2 M solution. By heating 2 mL of this solution at 140 °C for a few hours, a small MAPbI₃
462 crystal (<1 mm) is obtained. One small crystal is used as a seed and placed inside a fresh solution
463 and the crystal continues to grow into larger size. The seed crystal in the cavity is allowed to grow
464 for 3 days in a fresh precursor solution kept at 90 °C to obtain large (~1 cm) thin MAPbI₃ single

465 crystals. The crystals are then taken out and washed in Toluene. Finally, we polish the surface of
466 the crystal with SiC sandpaper followed by diamond paste polishing with grit size 3 μm , 1 μm and
467 0.25 μm , sequentially.

468 **Detector fabrication.** The polished thin MAPbI_3 crystals are transferred in an Argon filled
469 glovebox for device fabrication. For the hole selective contact, 50 μl of PTAA (10 mg/ml in CB)
470 is spin coated at 3000 rpm for 40 s on one side of the flat crystal followed by 100 nm of Au
471 deposition using e-beam. For the electron selective contact, 50 μl of PCBM (20 mg/ml in CB) is
472 spin coated at 3000 rpm for 40 s on the opposite side followed by thermal deposition of 5 nm BCP
473 and 100 nm of Pb. The hole/electron selective contacts do not affect the overall Schottky or Ohmic
474 contact behavior of the devices and may help improve the barrier height to suppress charge
475 injection from metal electrode into MAPbI_3 .

476 **Detector measurement setup.** The X-ray beam is generated by an X-ray tube with Ag target
477 (Amptek Mini-X X-ray tube) (see **Figure S8a** for X-ray energy spectrum). The device was located
478 at the axis of the X-ray beam with a distance ~ 20 cm where the X-ray dose rate in air was carefully
479 calibrated by a dosimeter (Fluke Biomedical RaySafe 452). For all measurements, the X-ray tube
480 is operated at a constant voltage of 30 kV. The X-ray dose rates in air at X-ray tube voltage of 30
481 kV and varying X-ray tube current are shown in **Figure S8b**. For detection limit measurements,
482 thin Aluminum sheets were added as attenuators between the device and the X-ray tube to reduce
483 the X-ray dose rate in air. The device current and voltage were measured by Keithley 4200A-SCS
484 parameter analyzer.

485 **Parameter estimation in the DL equations.** In the DL equations, (μ_1, σ_1^2) and (μ_2, σ_2^2) are
486 the true mean and true variance of the Group 1 and Group 2, respectively. The true means μ_1, μ_2

487 and true variances σ_1^2, σ_2^2 are estimated by respective sample means $\overline{X}_1, \overline{X}_2$ and sample variances
488 s_1^2, s_2^2 when measurements of the respective groups were performed.

489 **Normal distribution of the X-ray detector current.** The histogram of current counts vs
490 current was shown in **Figure S9**. The dark current of a Pb/Au device at 0V was measured to
491 eliminate the interference of dark current drift at non-zero bias voltage. Experimentally measured
492 current distribution supports the fundamental mathematical assumption that X-ray detector current
493 follows Normal distribution.

494

495

496

497

Supplementary Files

This is a list of supplementary files associated with this preprint. Click to download.

- [SupplementaryinfoDeterminationofXraydetectionlimitandapplicationinperovskiteXraydetectors.pdf](#)